Band Structure of the IV-VI Black Phosphorus Analog and Thermoelectric SnSe

I. Pletikosić,[1,2,*] F. von Rohr,[3] P. Pervan,[4] P. K. Das,[5,6] I. Vobornik,[5] R. J. Cava,[3] and T. Valla[2]

[1]*Department of Physics, Princeton University, Princeton, NJ 08544, USA*
[2]*Condensed Matter and Materials Science Department, Brookhaven National Laboratory, Upton, NY 11973, USA*
[3]*Department of Chemistry, Princeton University, Princeton, NJ 08544, USA*
[4]*Institut za fiziku, HR-10000 Zagreb, Croatia*
[5]*Istituto Officina dei Materiali (IOM-CNR), Laboratorio TASC, I-34149 Trieste, Italy*
[6]*International Centre for Theoretical Physics, I-34151 Trieste, Italy*

The success of black phosphorus in fast electronic and photonic devices is hindered by its rapid degradation in the presence of oxygen. Orthorhombic tin selenide is a representative of group IV-VI binary compounds that are robust and isoelectronic and share the same structure with black phosphorus. We measure the band structure of SnSe and find highly anisotropic valence bands that form several valleys having fast dispersion within the layers and negligible dispersion across. This is exactly the band structure desired for efficient thermoelectric generation where SnSe has shown great promise.

A growing interest in tin selenide emerged with the reporting of an unusually high thermoelectric figure of merit zT of 2.6 [1,2]. SnSe has also been considered as a prospective material for ultrathin photovoltaic films [3] and Li-ion battery anodes [4]. In addition, SnSe happens to be a group IV-VI (Sn, $5s^2 5p^2$; Se, $4s^2 4p^4$) isoelectronic analog of black phosphorus of group V (P, $3s^2 3p^3$). The sheets building black phosphorus, called phosphorene, have already shown great promise in fast-response electronic and photonic devices [5–10]. Sharing the almost defect-free two-dimensional structure with its flat cousin graphene, phosphorene displays relatively high charge carrier mobility [7,11,12] but, unlike graphene, has an inherent band gap, which, combined with various contact materials to offset the chemical potential, is essential for creating the on-off flow of electrons in digital logic, in the generation of photons in LEDs and lasers, or photon absorption in photovoltaics. The band gap of ultrathin black phosphorus films has also been shown to depend on the thickness and, with values of 0.3–2 eV, advantageously bridges the zero band gap of graphene and 1–2.5 eV gaps of transition metal dichalcogenides. Unfortunately, the material degrades within a few hours when exposed to oxygen and water vapor in air [13]. This is why related but stable layered semiconductors are of significant interest. The subject of this study, SnSe, shares a similar creased honeycomb layered crystal structure with black phosphorus, exhibits even higher carrier mobility, up to several thousand cm^2 V^{-1} s^{-1} [14–16], and like many similar layered materials can be exfoliated or epitaxially grown to yield films of definite atomic thickness [17–20]. SnSe, moreover, does not deteriorate in air. All this makes it a desirable isostructural, isoelectronic counterpart to black phosphorus.

The calculated band structure of SnSe has been reported in numerous density functional studies [2,21–33], with no experimental verification so far. Here, we report on features in the band structure of low-temperature SnSe we find important for the thermoelectric transport: pronounced anisotropy that results in a different response along the three crystal axes, valence band consisting of multivalley hole pockets, that are in turn capable of supporting highly mobile, low-effective-mass charge carriers. As some of these have not been precisely captured in existing *ab initio* simulations, our results will lead to a better understanding of both low- and high-temperature phases of this intriguing material.

Angle-resolved photoemission spectroscopy (ARPES) measurements were conducted at the APE beam line of Elettra Sincrotrone Trieste using a Scienta DA30 electron analyzer in the lens deflection mode that enables motion-free recording of the polar and tilt emission angles in the cone of a 30° opening. The azimuthal angle of the sample was fixed at the time of the mounting to the holder. The resulting momentum-space maps have been rotated by 22° to conveniently align the high-symmetry axes; the parts left out of the 30° cone were reconstructed by symmetrization. Photons in the range of 30–50 eV were used for the photoexcitation. The chemical potential of semiconducting samples was set to the position of the Fermi level ($0 = E_F$) of a nearby metallic sample. The temperature was held at 25 K.

SnSe was synthesized in an evacuated quartz tube from 5N tin shot and polished 3N5 selenium shot at 950 °C for 48 h. Single crystals were obtained by the vertical Bridgman method from a 950 °C melt of the fine powder of the resulting material enclosed in a 5 mm quartz tube that was drawn through the furnace at 0.2 mm/h.
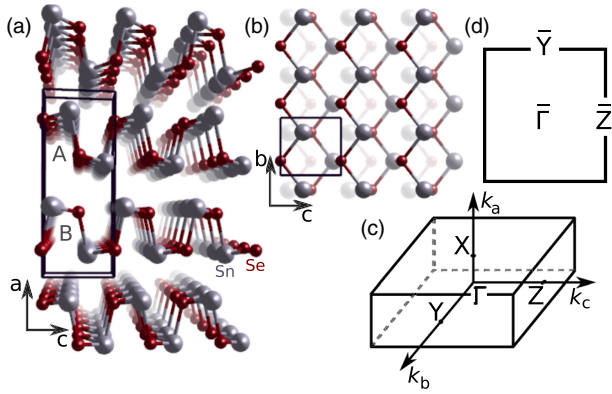
FIG. 1.   The crystal structure of SnSe viewed (a) along, and (b) perpendicular to the layers. The lower of the two layers contained in the unit cell, A and B, has in panel (b) been made nearly invisible. The unit cell size is $11.5 \times 4.2 \times 4.4$ Å^3. The reciprocal space repetition cells: (c) the three-dimensional bulk Brillouin zone with $\Gamma X = 0.27$ Å^{-1}, $\Gamma Y = 0.75$ Å^{-1}, $\Gamma Z = 0.71$ Å^{-1}; (d) the layer-bound two-dimensional surface Brillouin zone. The points Y and Z project along the a direction into $\bar{Y}$ and $\bar{Z}$, respectively.
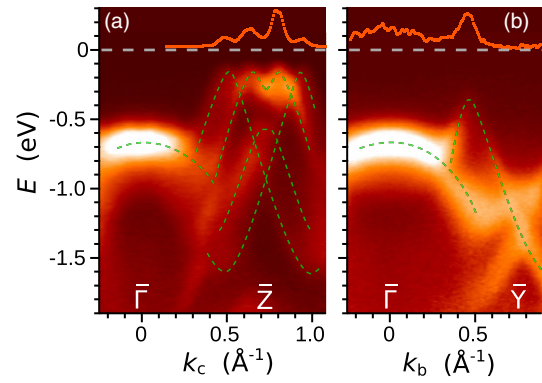

FIG. 2.   Photoemission spectral function showing the dispersion of the occupied electronic bands of SnSe along the high-symmetry directions (a) $\bar{\Gamma} - \bar{Z}$ and (b) $\bar{\Gamma} - \bar{Y}$ of the surface Brillouin zone. Dashed curves are tracing the bands that will be discussed in the text. The intensity profiles on top were taken at (a) -120 and (b) -350 meV. The photon energy was $h\nu = 34$ eV.

The crystal of SnSe consists of loosely bound layers that are, in the low-temperature phase ($T < 800$ K), built as an intricate knitting of tin and selenium atoms, in which each atom is linked to three of the other species by covalent bonds in trigonal pyramid geometry, forming distinct ridges along one of the crystal directions; see Figs. 1(a) and 1(b). The structure is such that a single layer, stretched into a flat sheet, would form a honeycomb lattice of alternating Sn and Se atoms. Neighboring layers are related by a center of inversion but are lacking one themselves [27].

We start by describing the electronic band structure along two high-symmetry directions of the in-plane momentum space. The photoemission spectra recorded using $h\nu = 34$ eV photons, displayed in Fig. 2, exhibit a multitude of downward dispersing bands at $\bar{\Gamma}$, from which several start rising in the direction of $\bar{Z}$ and one in the direction of $\bar{Y}$, reaching, however, a somewhat lower final energy before turning down again. The overlaid curves explicate the full band configuration. This has been deduced from a set of photon energy-dependent measurements, having the third component of the crystal momentum k_a span approximately one and a half bulk Brillouin zones (see Supplemental Material [34]).

When it comes to thermal and electronic transport properties of a material, they are in the valence band defined by the bands highest in energy and, thus, closest to the chemical potential. These will be discussed in more detail in what follows.

Figure 3 shows the momentum-space configuration of the highest lying bands in the occupied band structure. At -120 meV, four tiny collinear pockets, labeled $w_1 \ldots w_4$, start showing along $\bar{\Gamma} - \bar{Z}$ in the in-plane cut of the bulk

Brillouin zone [Fig. 3(a)]. The map was acquired using 38 eV photons, representing the perpendicular momentum (k_a) shift of about 0.15 Å^{-1} with respect to the spectra in Fig. 2. No shift of the band maxima can be resolved either in momentum (they are found on either side, 0.08 and 0.22 Å^{-1} away from $\bar{Z}$) or energy (ARPES intensity starts appearing at -120 meV). Only a change in relative intensities is observed when the intensity profile in Fig. 3(a) is compared to the profile on top in Fig. 2(a) and is most likely due to a variation in optical transition probabilities. Were the maximum energies that the neighboring bands $w_{1;3}$, $w_{2;4}$ reach different, their intensity profiles at constant energy would inevitably differ as well; that is not the case here. As the energy is lowered, the circular sections of these bands grow in size and soon merge. A gap of 250 meV opens up at $\bar{Z}$, marking the avoided crossing of the bands w_2 and w_4. Interestingly, no such gaps are observed at the crossings of the other two pairs—w_1,w_2 and w_4,w_3 in Figs. 2(a) and 3(b) or any of the figures in Ref. [34].

Two other hole pockets, labeled v_1 and v_2 in Fig. 3(b), emerge in the perpendicular direction, centered at $k_b = \pm 0.45$ Å^{-1} with apices below some -380 meV. Lastly, the first photoemission signatures of the circular bands around Γ become visible just below the energy of -600 meV.

Together with the almost negligible dispersion of the bands across the material's layers, that we observe in several other k_a cuts using a range of photon energies and show in Ref. [34], Fig. 3 adds to the notion of the unusual anisotropy of the band structure in all three crystal directions that can have significant consequences in many transport properties.

The effective mass and band velocity are the factors that decide the charge carrier mobility. In Fig. 4, we reexamine the two highest-lying hole pockets and determine the effective mass by fitting the band dispersion to parabolas locally centered at pocket maxima.
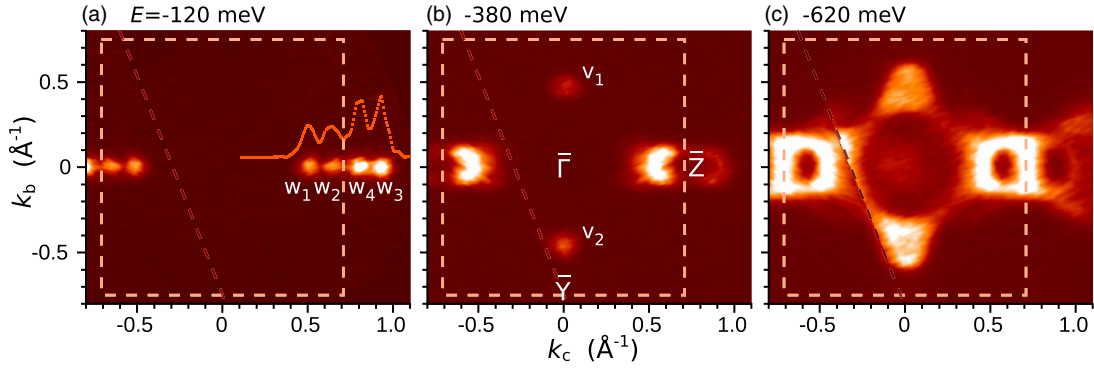
FIG. 3.   ARPES intensity maps in the momentum plane parallel to the layers of SnSe taken at the energies of (a) −120, (b) −380, and (c) −620 meV. The lower left corner of the maps was reconstructed by symmetrization from the opposite side. Photons of $h\nu = 38$ eV were used in (a); $h\nu = 50$ eV in (b) and (c). The dashed rectangles represent the surface Brillouin zone. Pockets along $\bar{\Gamma} - \bar{Z}$ received labels w_1–w_4; those along $\bar{\Gamma} - \bar{Y}$, v_1 and v_2.

Four hole pockets in the vicinity of $\bar{Z}$ appear to have very similar initial dispersion along the $\bar{\Gamma} - \bar{Z}$ direction [Fig. 4(a)]. Fitting to a parabola $(\hbar^2/2m)(k_c - k_w)^2$ for any of the apices w gives for the "effective mass" $m_c^w = 0.21 m_e$. The parabolic dispersion in the perpendicular direction [Fig. 4(b) is a cut for the second of the four] is slightly steeper, giving for the mass parameter of these pockets in the direction of k_b the value of $m_b^w = 0.18 m_e$. The fitting curves place the top of the valence band at 200 meV below the chemical potential. The pockets along the $\bar{\Gamma} - \bar{Y}$ direction are best visible in ARPES when the excitation energy of 50 eV is used (this represents a shift of 0.57 ± 0.03 Å^{-1} in k_a, to be compared to $2(\pi/a)$ of 0.54 Å^{-1}). Their cuts in two perpendicular in-plane directions are shown in Figs. 4(c) and 4(d). Parabolic fitting places the centroid of the intensity at 480 meV below the chemical potential. The pockets v have the effective mass of $m_c^v = 0.17 m_e$ in the c direction and $m_b^v = 0.24 m_e$ perpendicular to it. We show these summits and the fitting curves in greater detail in Fig. S3 in Ref. [34].

The key to the efficient generation of the electric power and the record-high zT of 2.6 in the high-temperature phase of SnSe ($T > 800$ K) is believed to be the unusually strong lattice anharmonicity and, consequently, a very low lattice thermal conductivity κ_l [1,35,36]. A similarly high zT of 2.0 was reported for p-doped single crystals in the low-temperature phase at 770 K. We will demonstrate here that the band structure of low-temperature SnSe has enough ingredients for a high thermopower, $PF = \sigma S^2$, and together with the inherently low thermal conductivity of the crystal should support the efficient power generation or cooling, as assessed by maximizing the figure of merit $zT = (\sigma S^2 / \kappa_e + \kappa_l)T$. Unfortunately, the parameters in this equation available for such an optimization—the electronic conductivity σ, the Seebeck coefficient S, and the electronic thermal conductivity κ_e—are interdependent and mutually opposing.

In order to achieve a high Seebeck voltage, the band structure around the chemical potential needs to act as a filter that favors the heat diffusion by either cold carriers below the chemical potential or hot carriers above and not
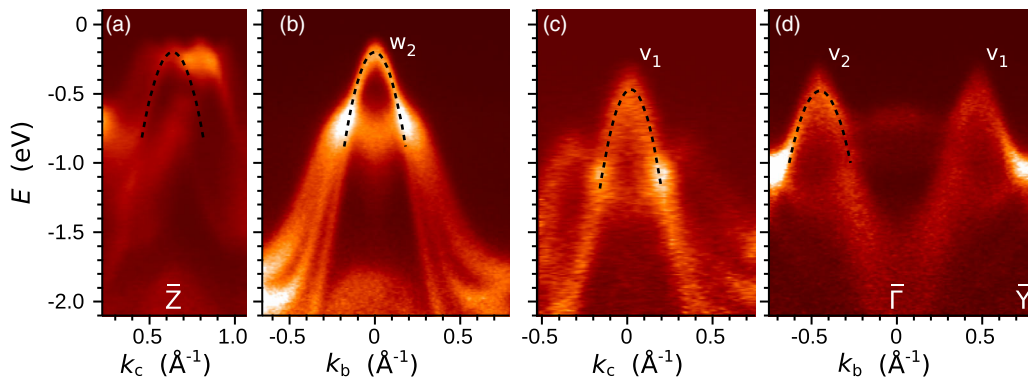

FIG. 4.   Energy dispersion cuts of the highest-lying pockets in the valence band structure of SnSe along two perpendicular directions in the momentum plane parallel to the layers. Panels (a) and (b) show the holelike pockets centered around $\bar{Z}$ and (c) and (d) the pockets in the vicinity of $\bar{Y}$. The bands are overlaid by parabolic fits used to estimate the effective mass. 34 eV photons were used in (a),(b) and 50 eV in (c),(d).

both equally at the same time [37]. That means having the chemical potential in the region of rapidly changing density of states or, better yet, in a semiconductor's gap closer to one and farther from the other extremum of the conduction and valence bands. With the predicted band gap of around 800 meV, and the valence band maximum at 200 meV below the chemical potential, our SnSe samples appear naturally p doped and thus well suited for voltage generation. We note, however, that part of the asymmetry at low temperatures is likely coming from unequal onsets of density of states at two ends of the gap and may change as the chemical potential shifts at higher T [21]. The higher voltage, in general, will be generated by a temperature gradient the farther in kT (at 600 K, $kT = 50$ meV) the chemical potential is from the extremum of the *conducting* band (that is, the valence band in p-doped or the conduction band in n-doped crystals). This unfortunately leads to a small carrier density n and reduced conductivity $\sigma = n\mu$ and severely lowers the available thermopower.

Tin selenide, as we have seen above, has in the low-energy occupied band structure a few fast-dispersing bands capable of hosting highly mobile carriers. Coupled with structural faultlessness, their high mobility (μ) can potentially balance out this reduced carrier density, providing enough conductivity for sizable thermopower.

Yet another feature works in favor of a high Seebeck coefficient in SnSe: The total band dispersion across the layers is extremely small. This implies a high effective mass m_a. Assuming a tight-binding form of dispersion along a, $E(k_b, k_c) - \Delta(1 - \cos ak_a)$, where 2Δ is below our detection limit of some 30–50 meV, we estimate m_a to be $2.5m_e$ or higher. When a thermal gradient is established along the layers, the uttermost value that the figure of merit can attain is expressed by the formula which summarizes the desired properties of an ideal thermoelectric material (Ref. [38]):

$$z_{\max} \propto \gamma \tau_{b|c} T^{3/2} \kappa_l^{-1} \sqrt{\frac{m_{c|b}}{m_{b|c}}} m_a.$$

The value is, fortuitously, proportional to m_a. When conduction along either b or c high-symmetry directions is assumed (the | above stands for *or*), the effective masses m_b and m_c that we determined to be of comparable size for a number of valence bands will in the above formula nearly cancel. Given the high anisotropy of the band structure, it should not be excluded that the ratio of the masses will increase when the two perpendicular in-plane directions are allowed to stray. The extreme in-plane band anisotropy of Fig. 3, not found in most but a few two-dimensional materials [39], may be detrimental to the electronic heat transport, as it limits the number of configurations available for the electrons to hop between in their random thermal motion. The anisotropy is also likely to affect the value of the scattering time τ of the carriers moving along the transport direction and should be considered when

optimizing the figure of merit as well. Interestingly enough, a recent angle-dependent conductivity study of SnSe finds the hole conductivity along b almost 4 times higher than along c [40]. The quasiparticle effective masses on top of the valence band, which we find almost equal in both in-plane directions, cannot account for the observed anisotropy. Our toy-model calculation, by the recipe of Ref. [24], for a single hole band having the dispersion of SnSe bands, indicates that the scattering times along the two directions should differ by an order of magnitude in order to reproduce the conductivity angular dependence [34]. This, curiously, does not lead to a notable Seebeck coefficient anisotropy and the power factor is affected only in the first order, through σ. Our model also nicely shows the benefits of having little out-of-plane dispersion: Power factor maxima are achieved for completely filled bands in the k_a direction and increase as the bands narrow.

Finally, the ingredient in the band structure of SnSe that can easily lead to doubling the figure of merit is the band degeneracy factor γ, which reflects the number of available modes in thermoelectric transport. We have found four hole pockets along $\bar{\Gamma} - \bar{Z}$ that appear at exactly the same energy in our constant energy maps [Fig. 3(a)] and have the same initial parabolic dispersion. This is an important finding that *ab initio* thermoelectric transport simulations should rely on.

Density functional studies of bulk SnSe [21–33] generally agree on the indirect nature of the band gap that forms between the valence band pockets along $\Gamma - Z$ and several electron pockets in the conduction band showing along $\Gamma - Y$. The electron pocket minima themselves, however, happen to be only a few tens of meV apart. Most studies underestimate by some 200–300 meV the size of the gap that was experimentally determined to be 860 meV [1]. They also underestimate the difference in energy of the valence band pockets w and v, that we establish at 280 meV, the difference ranging from 0 meV in Refs. [21,22] to 100–180 meV in Refs. [2,23–30]. The discrepancy is likely to affect the existing predictions of transport properties at any higher temperatures. There is also a disagreement in the number and nature of the pockets along $\Gamma - Z$: While the majority of studies show four, the bands do not always reach the same energy, and the 250 meV gap at $\bar{Z}$ due to the avoided crossing of the bands w_2 and w_4 never exists; most studies have it, however, between the pairs w_1, w_2 and w_4, w_3, where we, interestingly, observe none. Similar discrepancies exist for the effective masses, where calculations generally show a much higher variability than we have observed. *Ab initio* simulations tend to ascribe the anisotropy of the transport properties to the difference in the effective masses, mostly disregarding the anisotropy of the scattering time [40]. This all emphasizes the complexity of the band structure near band extrema and the sensitivity of band structure calculations that we are hoping to steer in the right direction. Our results will also help with the modeling and exploration of ultrathin layers of SnSe in search for advantageous properties already

found in black phosphorus—the band gap variable in size and (in)directionality [16,41–43] or enhancements of thermoelectric properties by band engineering and doping [2,33,43–47], spin-dependent transport in a single layer [27], or valleytronics by selective optical pumping from the valence to the conduction band valleys using linearly polarized light [48].

[*]ivop@princeton.edu

[1] L.-D. Zhao, S.-H. Lo, Y. Zhang, H. Sun, G. Tan, C. Uher, C. Wolverton, V. P. Dravid, and M. G. Kanatzidis, Nature (London) **508**, 373 (2014).

[2] L.-D. Zhao, G. Tan, S. Hao, J. He, Y. Pei, H. Chi, H. Wang, S. Gong, H. Xu, V. P. Dravid, C. Uher, G. J. Snyder, C. Wolverton, and M. G. Kanatzidis, Science **351**, 141 (2016).

[3] M. A. Franzman, C. W. Schlenker, M. E. Thompson, and R. L. Brutchey, J. Am. Chem. Soc. **132**, 4060 (2010).

[4] D.-H. Lee and C.-M. Park, ACS Appl. Mater. Interfaces **9**, 15439 (2017).

[5] S. P. Koenig, R. A. Doganov, H. Schmidt, A. H. Castro Neto, and B. Özyilmaz, Appl. Phys. Lett. **104**, 103106 (2014).

[6] F. Xia, H. Wang, and Y. Jia, Nat. Commun. **5**, 4458 (2014).

[7] L. Li, Y. Yu, G. J. Ye, Q. Ge, X. Ou, H. Wu, D. Feng, X. H. Chen, and Y. Zhang, Nat. Nanotechnol. **9**, 372 (2014).

[8] H. Liu, A. T. Neal, Z. Zhu, Z. Luo, X. Xu, D. Tománek, and P. D. Ye, ACS Nano **8**, 4033 (2014).

[9] M. Buscema, D. J. Groenendijk, S. I. Blanter, G. A. Steele, H. S. J. van der Zant, and A. Castellanos-Gomez, Nano Lett. **14**, 3347 (2014).

[10] A. Carvalho, M. Wang, Xi Zhu, A. S. Rodin, H. Su, and A. H. Castro Neto, Nat. Rev. Mater. **1**, 16061 (2016).

[11] J. Qiao, X. Kong, Z.-X. Hu, F. Yang, and W. Ji, Nat. Commun. **5**, 4475 (2014).

[12] G. Long, D. Maryenko, J. Shen, S. Xu, J. Hou, Z. Wu, W. K. Wong, T. Han, J. Lin, Y. Cai, R. Lortz, and N. Wang, Nano Lett. **16**, 7768 (2016).

[13] Y. Huang, J. Qiao, K. He, S. Bliznakov, E. Sutter, X. Chen, D. Luo, F. Meng, D. Su, J. Decker, W. Ji, R. S. Ruoff, and P. Sutter, Chem. Mater. **28**, 8330 (2016).

[14] M. M. Nassary, Turk. J. Phys. **33**, 201 (2009).

[15] H. Maier and D. R. Daniel, J. Electron. Mater. **6**, 693 (1977).

[16] L.-C. Zhang, G. Qin, W.-Z. Fang, H.-J. Cui, Q.-R. Zheng, Q.-B. Yan, and G. Su, Sci. Rep. **6**, 19830 (2016).

[17] L. Li, Z. Chen, Y. Hu, X. Wang, T. Zhang, W. Chen, and Q. Wang, J. Am. Chem. Soc. **135**, 1213 (2013).

[18] H. Ju and J. Kim, ACS Nano **10**, 5730 (2016).

[19] C. Zhang, H. Zin, M. Han, Z. Dai, H. Pang, Y. Zheng, Y-Q. Lan, J. Bao, and J. Zhu, ACS Nano **8**, 3761 (2014).

[20] X. Li, M. W. Lin, A. A. Puretzky, J. C. Idrobo, C. Ma, M. Chi, M. Yoon, C. M. Rouleau, I. Kravchenko, D. B. Geohegan, and K. Xiao, Sci. Rep. **4**, 5497 (2014).

[21] A. J. Hong, L. Li, H. X. Zhu, Z. B. Yan, J. M. Liu, and Z. F. Ren, J. Mater. Chem. A **3**, 13365 (2015).

[22] H. I. Sirikumara and T. Jayasekera, J. Phys. Condens. Matter **29**, 425501 (2017).

[23] L. C. Gomes and A. Carvalho, Phys. Rev. B **92**, 085406 (2015).

[24] R. L. González-Romero, A. Antonelli, and J. J. Meléndez, arXiv:1612.05967v1.

[25] K. Kutorasinski, B. Wiendlocha, S. Kaprzyk, and J. Tobola, Phys. Rev. B **91**, 205201 (2015).

[26] H. Mori, H. Usui, M. Ochi, and K. Kuroki, Phys. Rev. B **96**, 085113 (2017).

[27] G. Shi and E. Kioupakis, Nano Lett. **15**, 6926 (2015); J. Appl. Phys. **117**, 065103 (2015).

[28] Y. Suzuki and H. Nakamura, Phys. Chem. Chem. Phys. **17**, 29647 (2015).

[29] J. Yang, G. Zhang, G. Yang, C. Wang, and Y. X. Wang, J. Alloys Compd. **644**, 615 (2015).

[30] R. Guo, X. Wang, Y. Kuang, and B. Huang, Phys. Rev. B **92**, 115202 (2015).

[31] H. Yu, S. Dai, and Y. Chen, Sci. Rep. **6**, 26193 (2016).

[32] G. Ding, G. Gao, and K. Yao, Sci. Rep. **5**, 9567 (2015).

[33] A. Shafique and Y.-H. Shin, Sci. Rep. **7**, 506 (2017).

[34] See Supplemental Material at http://link.aps.org/supplemental/10.1103/PhysRevLett.120.156403 for photon energy-dependent spectra and anisotropic scattering one-band model of conduction in SnSe.

[35] J. Carrete, N. Mingo, and S. Curtarolo, Appl. Phys. Lett. **105**, 101907 (2014).

[36] C. W. Li, J. Hong, A. F. May, D. Bansal, S. Chi, T. Hong, G. Ehlers, and O. Delaire, Nat. Phys. **11**, 1063 (2015).

[37] S. Datta, M. Lundstrom, and A. Shakouri, nanoHUB.org, Thermoelectricity: From Atoms to Systems (unpublished).

[38] J. R. Sootsman, D. Y. Chung, and M. G. Kanatzidis, Angew. Chem., Int. Ed. **48**, 8616 (2009).

[39] I. Pletikosić, M. N. Ali, A. V. Fedorov, R. J. Cava, and T. Valla, Phys. Rev. Lett. **113**, 216601 (2014).

[40] X. Xu, Q. Song, H. Wang, P. Li, K. Zhang, Y. Wang, K. Yuan, Z. Zang, Y. Ye, and L. Dai, ACS Appl. Mater. Interfaces **9**, 12601 (2017).

[41] S.-D. Guo and Y.-H. Wang, J. Appl. Phys. **121**, 034302 (2017).

[42] C. Kamal, A. Chakrabarti, and M. Ezawa, Phys. Rev. B **93**, 125428 (2016).

[43] F. Q. Wang, S. Zhang, J. Yu, and Q. Wang, Nanoscale **7**, 15962 (2015).

[44] H. Zhu, W. Sun, R. Armiento, P. Lazic, and G. Ceder, Appl. Phys. Lett. **104**, 082107 (2014).

[45] A. T. Duong, V. Q. Nguyen, G. Duvjir, V. T. Duong, S. Kwon, J. Y. Song, J. K. Lee, J. E. Lee, S. Park, T. Min, J. Lee, J. Kim, and S. Cho, Nat. Commun. **7**, 13713 (2016).

[46] M. Gharsallah, F. Serrano-Sánchez, N. M. Nemes, F. J. Mompeán, J. L. Martínez, M. T. Fernández-Díaz, F. Elhalouani, and J. A. Alonso, Sci. Rep. **6**, 26774 (2016).

[47] Y. Pei, H. Wang, and G. J. Snyder, Adv. Mater. **24**, 6125 (2012).

[48] A. S. Rodin, Lidia C. Gomes, A. Carvalho, and A. H. Castro Neto, Phys. Rev. B **93**, 045431 (2016).